MOLECULAR GAS DYNAMICS OF THE STRONGLY-LENSED WET-MERGER RXS J1131−1231 AT Z=0.654

T. K. Daisy Leung and Dominik A. Riechers

Department of Astronomy, Space Sciences Building, Cornell University, Ithaca, NY 14853, USA; tleung@astro.cornell.edu

To be submitted to the ApJ

ABSTRACT

We present interferometric observations of $CO(J = 2 \rightarrow 1)$ and $CO(J = 3 \rightarrow 2)$ emission toward the "Einstein ring" RXS J1131−1231 at $z = 0.654$, obtained with the Plateau de Bure Interferometer and Combined Array for Research in Millimeter-wave Astronomy. RXJ1131 is gravitationally lensed quasar. Spatially and spectrally resolved. This is the first resolved $CO(J = 2 \rightarrow 1)$ imaging at intermediate redshift. The molecular gas of $M_{\rm gas} = 123 BLAH \times 10^{10} \, M_\odot$ in the host galaxy is extended (~ 6 kpc). An optically faint companion galaxy with gas mass BLAH (gas mass ratio 1:7). RXS J1131-1231 a wet-merger, Dynamical lens modeling, the intrinsic dynamics and blah are suggestive of a rotating disk morphology , consistent with previous results based on optical observations. is indicative of, and suggests... The gas mass fraction of $\sim 19\%$, consistent with the trend of decreasing gas fraction at this epoch.

Subject headings: ISM: molecular – infrared: galaxies – galaxies: mergers – galaxies: starburst – galaxies: evolution

1. INTRODUCTION

Studies of galaxy evolution have been focusing on the interplay between baryonic physics (e.g., feedback and gas dissipation) and star formation and active galactic nucleus (AGN) activity across cosmic epochs. It is not well-understood when and how baryons of present-day galaxies were assembled, but it is clear that both the co-moving star formation rate and black hole accretion rate densities increased substantially since $z > 3$ and reached their climax at $z \sim 2$, followed by a rapidly decline toward $z \sim 0$ (e.g., Hopkins & Beacom 2006; Madau & Dickinson 2014). A leading explanation for this decline is related to the evolution of molecular gas content and star formation efficiency (Erb et al. 2006; Carilli & Walter 2013; Walter et al. 2014), but confirmation from direct molecular gas measurements at intermediate redshift ($0.2 < z < 1$) is still limited both in number and in the variety of galaxy populations probed — only unresolved CO observations have been carried out for ~ 70 ULIRGs up to date (Combes et al. 2011, 2013).

In the current paradigm, it is posited that every nearby, massive galaxy host a supermassive black hole (SMBH), which grows by accretion of the cold molecular gas from its host galaxy. Meanwhile, empirical scaling relations such as the Magorrian relation (Magorrian et al. 1998) — a tight correlation between black hole mass and stellar bulge mass — have been established locally, implying a self-regulating co-eval growth between local SMBHs and their host galaxies. Attempts to extend this relation out to higher redshifts, beyond the peak epoch of star formation and AGN activity, have been made in recent years. It has been reported that the $M_{\rm BH}/M_{\rm bulge}$ ratio of high-z sub-millimeter galaxies (SMGs) falls below the local relation (e.g., Borys et al. 2005; Alexander et al. 2008) but that of high-z quasar host galaxies are found lying above the relation (e.g., McLure et al. 2006; Peng et al. 2006). Stellar mass of quasar host galaxies at $z > 4$ constrained by their

CO-based dynamical mass are also too small compared to that based from the local relation (Walter et al. 2004; Riechers et al. 2008; Coppin et al. 2008). It is evident that high-z galaxies deviates from the local relation, and among their galaxy populations, but the AGN-host galaxy connection at intermediate redshift is still poorly-constrained. This owes to the difficulties in measuring stellar emission in the host galaxy under the presence of a bright quasar, or alternatively owing to the lack of spatially resolved CO observations to provide dynamical constraints on the stellar mass. With gravitational lensing, emission of the background quasar and its host galaxy is magnified and stretched out to different extents, and is projected to different locations in the image plane. This in effect increases the surface brightness contrast between their emission and allows for the relatively uncontaminated measurements of their emission.

The "Einstein ring" RXS J113151.62−123158 (hereafter RXJ1131) at $z_{\rm s, QSO} = 0.685$ (Sluse et al. 2003, hereafter S03) is a particularly well-suited source for studying the evolution of molecular gas properties in quasar host galaxies and the connection between SMBHs and their host galaxies at intermediate redshift given its unique lensing configuration and its redshift. The stellar emission in the host galaxy of RXJ1131 is lensed into an Einstein ring of radius $1''83$ that is clearly separated from the quadruply imaged quasar emission (Claeskens et al. 2006, hereafter C06). We have thus carried out a detailed study for RXJ1131, as presented in this paper. RXJ1131 is strongly lensed by an elliptical galaxy at $z_{\rm L} = 0.295$ (S03). The black hole residing in RXJ1131 is rotating with a high spin parameter ($a \sim 0.9$; Reis et al. 2014). Previous studies also report a black hole mass of $M_{\rm BH} < 2 \times 10^8 M_\odot$[1].

---

[1] Various values for the black hole mass have been reported based on the different methods and normalizations used. Dai et al. (2010) find a $M_{\rm BH}$ $\sim 10^8 M_\odot$ using the virial estimator with Hβ linewidth, and Pooley et al. (2007) report $M_{\rm BH} = 2.5 \times 10^7 M_\odot$ using the AGN bolometric luminosity of

This paper is structured as follows. In §2, we outline the details of the observations and our data reduction process. In §3, we describe our astrometric corrections applied to align an *HST* image with our radio maps. In §4, we report measurements of the CO($J = 2 \rightarrow 1$) and CO($J = 3 \rightarrow 2$) lines and a compilation of photometric data from optical to radio wavelengths. In §5, we present dynamical lens modeling of the CO($J = 2 \rightarrow 1$) data, SED modeling of the thermal dust continuum, and the resulting physical properties inferred for RXJ1131. In §6, we discuss the merger stage of RXJ1131, and the implications of this study in the context of the evolution of molecular gas content and the M_{BH}–M_{dyn} relation at intermediate redshift. Finally, we summarize the main results and present our conclusions in §7. We use a concordance ΛCDM cosmology throughout this paper, with parameters from the WMAP9 results: $H_0 = 69.32$ km s^{-1} Mpc^{-1}, $\Omega_M = 0.29$, and $\Omega_\Lambda = 0.71$ (Hinshaw et al. 2013).

2. OBSERVATIONS

2.1. *PdBI CO(J = 2 → 1)*

Observations of the CO($J = 2 \rightarrow 1$) rotational line ($\nu_{rest} = 230.5379938$ GHz) redshifted to $\nu_{obs} = 139.0$ GHz were carried out using IRAM Plateau de Bure Interferometer (PdBI; Program ID: S14BX; PI: D. Riechers). Two observing runs were carried out on 2014 December 06 and 2015 February 05 under good weather conditions in the C and D array configurations, respectively. The 2 mm receivers were used to cover the redshifted CO($J = 2 \rightarrow 1$) line and the underlying continuum emission, employing a correlator setup providing an effective bandwidth of 3.6 GHz (dual polarization) and a spectral resolution of 10.0 MHz (~ 21.5 km s^{-1}). This resulted in 3.75 hours of cumulative six antenna-equivalent on-source time after discarding unusable visibility data. The nearby quasars B1127−145 and B1124−186 were observed every 22 minutes for pointing, secondary amplitude, and phase calibration, and B1055+018 was observed as the bandpass calibrator for both tracks. MWC349 and 3C279 were observed as primary flux calibrators for the C and D array observations, respectively, yielding ≲15% calibration accuracy.

The GILDAS package was used to reduce and analyze the visibility data. The calibrated visibility data were imaged and deconvolved using the CLEAN algorithm with "natural" weighting. This yields a synthesized clean beam size of $4\rlap{.}''44 \times 1\rlap{.}''95$ (PA = 13°). The final rms noise is $\sigma = 1.45$ mJy beam^{-1} over 10 MHz (21.5 km s^{-1}). The continuum image at $\nu_{cont} \sim 139$ GHz is created by averaging over 3.16 GHz of line-free bandwidth. This yields an rms noise of 0.082 mJy beam^{-1}.

2.2. *CARMA CO(J = 3 → 2)*

Observations of the CO($J = 3 \rightarrow 2$) rotational line in RXJ1131 ($\nu_{rest} = 345.7959899$ GHz) redshifted to $\nu_{obs} = 208.6$ GHz were carried out with the Combined Array for Research in Millimeter-wave Astronomy

$L_{bol,X} = 1.3 \times 10^{45}$ ergs s^{-1}, assuming $L/L_{Edd} = 0.25$ and $\eta = 0.15$.

(CARMA; Program ID: cf0098; PI: D. Riechers) in the D array configuration on 2014 February 02 under poor 1.5 mm weather conditions and on 2014 February 17 under good 1.5 mm weather conditions. The correlator setup provides a bandwidth of 3.75 GHz in each sideband and a spectral resolution of 12.5 MHz (~ 17.9 km s^{-1}). The line was placed in the lower sideband with the local oscillator tuned to $\nu_{LO} \sim 216$ GHz. The radio quasars J1127−189 (first track) and 3C273 (second track) were observed every 15 minutes for pointing, amplitude, and phase calibration. Mars was observed as the primary absolute flux calibrator and 3C279 was observed as the bandpass calibrator for both tracks. This results in a total on-source time of 2.94 hours after flagging poor visibility data.

Given that the phase calibrator used for the first track was faint and was observed under poor weather conditions and that the phase calibrator used for the second track was far from our target source, the phase calibration is subpar, with an rms scatter $\sim 60°$ over a baseline length of ~ 135 m. We thus conservatively estimate a calibration accuracy of $\sim 45\%$ based on the flux scale uncertainties, the gain variations over time, and the phase scatter on the calibrated data. We therefore treat its line intensity with caution and ensure that our physical interpretation of this system and the conclusion of this do not rely on this quantity.

The MIRIAD package was used to calibrate the visibility data. The calibrated visibility data were imaged and deconvolved using the CLEAN algorithm with "natural" weighting. This yields a synthesized clean beam size of $3\rlap{.}''2 \times 1\rlap{.}''9$ (PA = 8°) for the lower sideband image cube. The final rms noise is $\sigma = 13.3$ mJy beam^{-1} over a channel width of 25 MHz. An rms noise of $\sigma = 0.83$ mJy beam^{-1} is reached by averaging over the line-free channels.

2.3. *VLA (Archival)*

Our analysis also uses archival data of the 5 GHz radio continuum obtained with the Very Large Array (VLA; Program ID: AW741; PI: Wucknitz). Observations were carried out on 2008 December 29 under excellent weather conditions in the A array configuration for a total of ~ 7 hours on-source time. The C-band receivers were used with a continuum mode setup, providing a bandwidth of 50 MHz for the two IF bands with full polarization. The nearby radio quasar J1130−149 was observed every 10 minutes for pointing, amplitude, and phase calibration, J1331+305 was observed as the primary flux calibrator, and J0319+415 was observed as the bandpass calibrator, yielding $\sim 10\%$ calibration accuracy. We used AIPS to calibrate the visibility data. The calibrated visibility data were imaged and deconvolved using the CLEAN algorithm using robust = 0. This yields a synthesized clean beam size of $0\rlap{.}''49 \times 0\rlap{.}''35$ (PA = 0.18°) and a final rms noise of $\sigma = 13$ μJy beam^{-1}.

3. HST ASTROMETRY

We obtained an *HST* image taken with the ACS/Wide Field Camera using the F555W filter (*V*-band) from the

Hubble Legacy Archive[2]. The details of the observations can be found in C06. We adopt the VLA 5 GHz map as the reference coordinate frame to align the optical (V-band) image. We shift the latter to the east by $0.''5963$ in R.A. and $+0.''8372$ in Dec., which is consistent with the typical astrometric precision ($1''$–$2''$) of images from the Hubble Legacy Archive[3]. This astrometric correction is critical to avoid artificial spatial offsets between different emitting regions and to carry out our lens modeling, in which the absolute position of the foreground lensing galaxy is guided by its coordinates in the optical image, where its emission is clearly detected. The VLA image is calibrated using a well-monitored phase calibrator, with absolute positional accuracy of ~2 mas. For this reason, the absolute alignment between the VLA image and other interferometric images reported in this paper are expected to have an astrometric precision better than $0.''1$, modulo uncertainties related to the SNR and phase instability.

4. RESULTS

4.1. *CO(J = 2 → 1) Emission*

We detect CO($J = 2 \rightarrow 1$) line emission toward the background source at $\gtrsim 27\sigma$ significance, confirming the redshift at $z_{\rm CO} = 0.65370 \pm 0.0005$. The emission is spatially and dynamically resolved with a highly asymmetric double-horned line profile as shown in Figure 1. Fitting a double Gaussian results in peak flux densities of 75.3 ± 2.6 and 24.0 ± 2.0 mJy, and a FWHM of 179 ± 9 km s^{-1} and 255 ± 28 km s^{-1} for the two components, respectively. The peaks are separated by $\Delta v_{\rm sep} = 400 \pm 12$ km s^{-1}. The total integrated line flux is 24.1 ± 2.3 Jy km s^{-1}.
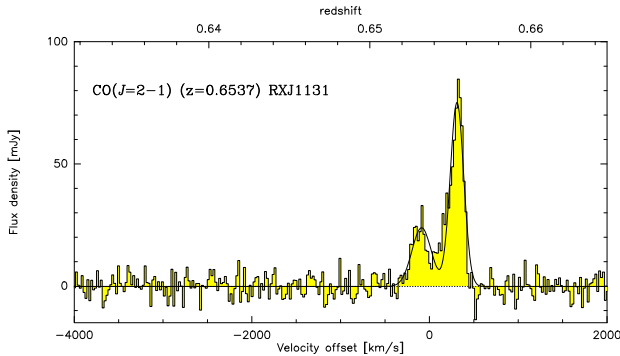

FIG. 1.— Spectrum of CO($J = 2 \rightarrow 1$) emission toward RXJ1131. The velocity scale is with respect to $z = 0.6537$, which is approximately the line center considering the asymmetry as a result of differential lensing. A detailed discussion of this effect is presented in §5.1.2.

We construct the zeroth moment map, a red/blue channel map, and the first and second moment maps in Figure 2 using the uv-continuum subtracted data cube over a velocity range of $\Delta v \sim 750$ km s^{-1}. The higher-order moment maps are created using unbinned channel maps with 3σ

clipping. The peak flux density is 8.12 ± 0.30 Jy km s^{-1} beam^{-1} in the intensity-integrated map.

The deconvolved source size FWHM from fitting a two-dimensional Gaussian is $5.''1 \pm 0.''72 \times 3.''72 \pm 0.''66$, and thus, the emission is resolved over ~2.2 beams. While the lensed emission is not strictly distributed as a two-dimensional Gaussian; the fit recovers the line intensity enclosed by the emitting region, we therefore take this as an estimate on the extent of the lensed emission. On the other hand, if we assume that the spatial distribution of the lensed molecular gas emission is similar to that in the optical to near-IR wavelengths, the lensed emission would be more accurately described by an annulus, enclosing the partially complete "Einstein ring" and the lensed knots (see Figure 2).

We also place an upper limit on HNC($J = 2 \rightarrow 1$) line emission in the foreground galaxy at $z \sim 0.295$. Assuming a typical line width of 300 km s^{-1}, this corresponds to a 3σ limit of 0.35 Jy km s^{-1} beam^{-1}.

4.2. *CO(J = 3 → 2) Emission*

We detect CO($J = 3 \rightarrow 2$) line emission toward RXJ1131 at **BLAH**σ significance. The spectrum is shown in Figure 3, which appears to be consistent with a double-peaked profile. We estimate a line intensity of 35.7 ± 21.9**BLAH** Jy km s^{-1} by summing up fluxes over the FWZI linewidth used to infer the CO($J = 2 \rightarrow 1$) line intensity (~700 km s^{-1}). Assuming the spatial extent between CO($J = 2 \rightarrow 1$) and CO($J = 3 \rightarrow 2$) are similar and therefore magnified by the same amount, the line intensities correspond to a brightness temperature ratio of $r_{32} = T_{{\rm CO}(J = 3 \rightarrow 2)} / T_{{\rm CO}(J = 2 \rightarrow 1)} = 0.66 \pm 0.41$.

4.3. *Continuum Emission*

No 1.5 mm continuum emission is detected at the position of CO($J = 3 \rightarrow 2$) down to a 3σ limit of 2.49 mJy beam^{-1}. This is consistent with the spectrum shown in Figure 3.

We detect PdBI 2 mm continuum in Figure 4. The integrated flux density is 1.2 ± 0.2 mJy, with a peak flux $S_\nu = 800 \pm 88\ \mu$Jy beam^{-1} centered on the lensing galaxy. Slightly extended emission is also detected along the lensed arc. This suggests that the detected emission comes from both the foreground galaxy and the background galaxy and that the emission is marginally resolved along its major axis. We subtract a point source model in uv-plane to remove the unresolved emission toward the foreground galaxy. The peak flux (0.39 ± 0.08 mJy) in the residual map coincides with the lensed arc, and is consistent with the difference between the integrated and peak flux in the original continuum map (~0.4 mJy). We therefore adopt $S_\nu = 0.39 \pm 0.08$ mJy as the 2 mm continuum emission toward the background galaxy.

The VLA C-band continuum image in Figure 4 shows resolved emission from the jets and core of the foreground elliptical galaxy as well as emission toward the background quasar. Multiple peaks are seen along the arc with their centroids coincident with the optical emission from the quasar. We extract the flux densities for
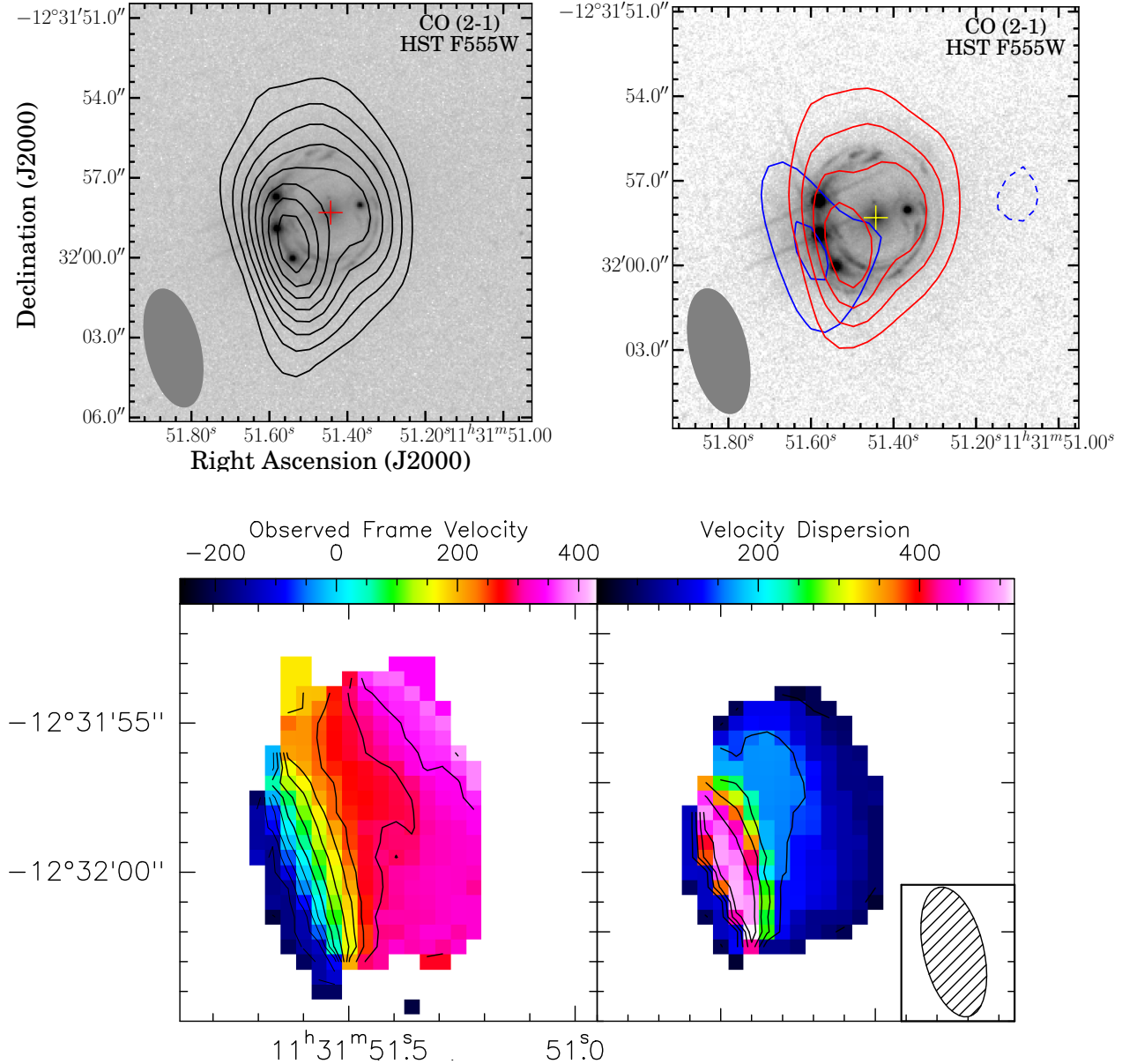
FIG. 2.— Top left: overlay of the velocity-integrated CO($J = 2 \rightarrow 1$) emission on the archival *HST V*-band (F555W) image. Top right: same as top left, except the contours are color-coded to represent the red- and blueshifted emission. The contours in both top panels start at 3σ and increment at steps of $\pm 3\sigma$, where $\sigma = 0.3$ mJy beam^{-1} for the top left panel, and $\sigma = 0.4$ mJy beam^{-1} (red) and 0.5 mJy beam^{-1} (blue) for the top right panel. The crosses denote the location of the foreground galaxy at $z = 0.295$. Contours for the first (bottom left) and second (bottom right) moment maps of the CO($J = 2 \rightarrow 1$) line emission are shown in steps of 50 km s^{-1}, and 100 km s^{-1}, respectively. The synthesis beam size is $4.''4 \times 2.''0$, at PA = 13°.

the lensing arc and the radio core in Table 1. We find a spectral index of $\alpha_{6cm}^{2mm} = -0.024$ for the foreground galaxy and $\alpha_{6cm}^{2mm} = -0.345$ for the background galaxy by fitting a power-law ($S_\nu \propto \nu^\alpha$) to the continuum emission at 5 GHz and 2 mm.

4.4. *Photometry*

We compile mid-IR (MIR) to far-IR broadband photometry from various catalogs available on the NASA/IPAC Infrared Science Archive (IRSA) in Table 1 with aperture corrections when warranted. These data were obtained using the Two Micron All Sky Survey Telescopes (2MASS; Skrutskie et al. 2006), the Wide-field Infrared Survey Explorer (*WISE*; Wright et al. 2010), the *Infrared Astronomi-*

cal Satellite (*IRAS*; Neugebauer et al. 1984), and the Multiband Imaging Photometer (MIPS; Rieke et al. 2004) and Mid-infrared Infrared Array Camera (IRAC; Fazio et al. 2004) on the *Spitzer Space Telescope*. We retrieve PBCD (level 2) *Spitzer*/IRAC images from the Spitzer Heritage Archive and perform aperture photometry on the channel 1 image to extract the flux density at 3.6 μm since it is not available from the IRSA archive.

The emission in the IRAC images is slightly extended. We thus use the *HST* image ($\sim 0.''07$ resolution) to determine origins of their centroids, all of which are found to be centered at the position corresponding to the lensed emission from the background galaxy. To recover the diffuse background emission, we subtract a point source model
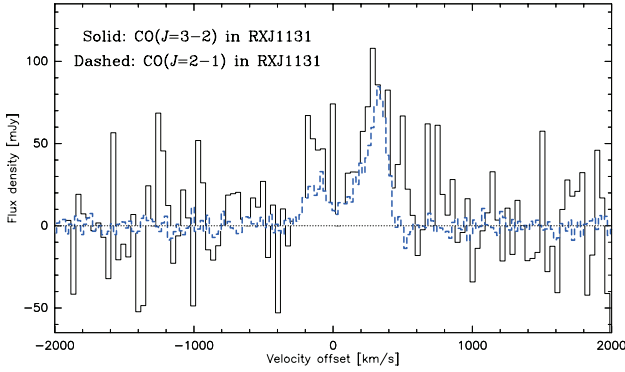
FIG. 3.— CARMA CO($J = 3 \rightarrow 2$) line profile (solid) without continuum subtraction is over-plotted on the continuum-subtracted PdBI CO($J = 2 \rightarrow 1$) line profile (dashed). The velocity scale is with respect to $z = 0.6537$, which corresponds to the dynamical center of the CO($J = 2 \rightarrow 1$) line. The spectral resolution for CO($J = 3 \rightarrow 2$) and CO($J = 2 \rightarrow 1$) is 35.8 km s^{-1} and 21.5 km s^{-1}, respectively.

centered on the lensing galaxy, using the average FWHM found by fitting a Gaussian profile to several field stars with the IMEXAM routine of IRAF. We perform aperture photometry on the residual image to obtain decomposed flux measurements from the background galaxy. The photometry for the foreground galaxy is then obtained by subtracting the background emission from the observed total flux. The resulting photometry in Table 1 are obtained after performing an aperture correction described in the IRAC Instrument Handbook[4] to correct for the fact that the imaging was calibrated using a 12″ aperture, which is larger than the aperture (5.″8) we used to perform aperture photometry.

We fit a power-law spectrum to the decomposed IRAC photometry to disentangle the background and foreground emission from the total flux observed in the MIPS 24 μm band. The spectral indices corresponding to best-fitting curves are $\alpha = -1.8$ and $\alpha = -0.85$ for the lensing galaxy and RXJ1131, respectively. The latter is consistent with the mean $3.6 - 8\,\mu$m spectral slope of $\alpha = -1.07 \pm 0.53$ found for unobscured AGN (Stern et al. 2005). An extrapolation of the fit to 24 μm yields 33.96 ± 0.01 mJy and 25.19 ± 0.03 mJy for the foreground galaxy and RXJ1131, respectively. The uncertainties are the standard deviations of the extrapolated fluxes obtained from two independent Monte Carlo simulations, each of 500 iterations. We incorporate the decomposed 24 μm data in our SED fitting to provide some constraints on the Wien tail beyond the dust peak of the spectral energy distribution (SED) of RXJ1131. Details of the SED modeling are presented in §5.4.

Extraction of the *Herschel*/SPIRE photometry at 250, 350, and 500 μm was carried out using SUSSEXTRACTOR within the Herschel Interactive Processing Environment (HIPE; Ott 2010) on Level 2 maps obtained from the Herschel Science Archive. These maps were processed by the SPIRE pipeline version 13.0 within HIPE. The SUSSEXTRACTOR task estimates the flux density from an image convolved with a kernel derived from the SPIRE beam. The flux density measured by SUSSEXTRACTOR is addi-

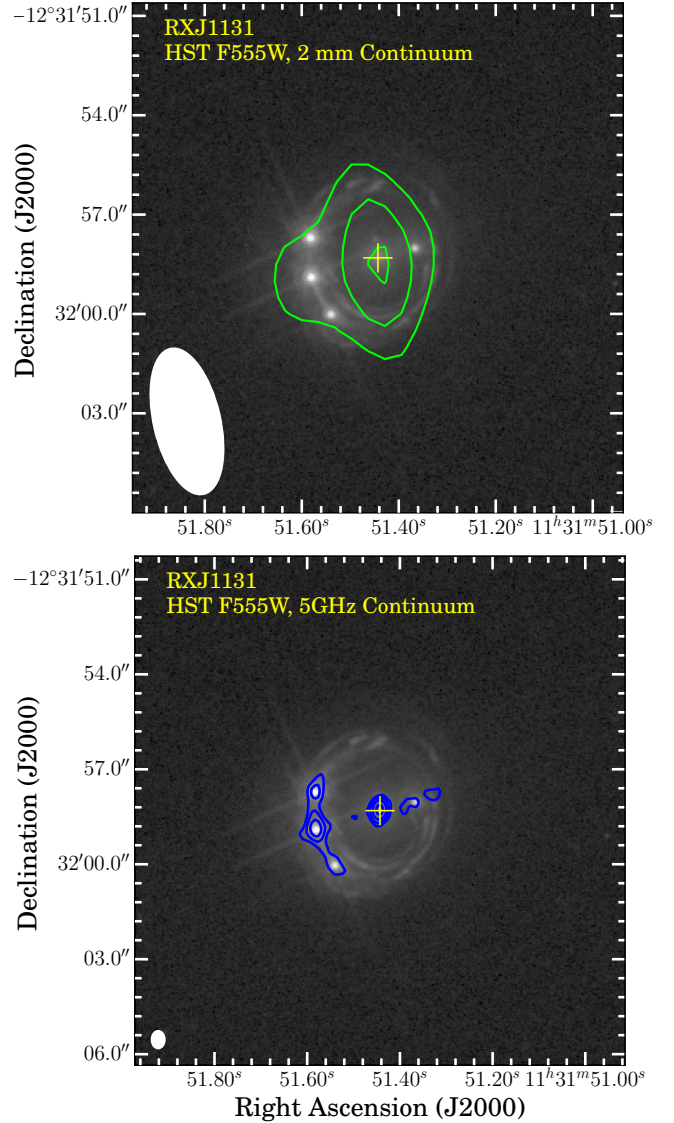4 http://irsa.ipac.caltech.edu/data/SPITZER/docs/irac/iracinstrumenthandbook/

FIG. 4.— Top: overlay of the 2 mm continuum emission on the optical image. Bottom: overlap of the VLA 5 GHz continuum emission on the optical image. Contours in both images start and increment at steps of $\pm 3\sigma$, where $\sigma_{2mm} = 0.082$ mJy beam^{-1} and $\sigma_{5GHz} = 13\,\mu$Jy beam^{-1} in the top and bottom panel, respectively. The central crosses indicate the centroid of the foreground galaxy, as detected in the optical image. The synthesis beam size is $4.''4 \times 2.''0$, at PA = 13° for the PdBI observations (top), and $0.''5 \times 0.''4$ (PA = 0.18°) for the VLA observations (bottom).

tionally confirmed using the Timeline Fitter, which performs photometry by fitting a 2D elliptical Gaussian to the Level 1 data at the source position given by the output of SUSSEXTRACTOR. The fluxes obtained from both methods are consistent within the uncertainties.

5. ANALYSIS

5.1. *Lens Modeling*

At the angular resolution of the CO($J = 2 \rightarrow 1$) data, the images are resolved over ∼2 resolution elements. Given the extent of the lensed emission (see Figure 2), this implies that we do not resolve structures (e.g. knots and arcs) of the lensed emission in our CO($J = 2 \rightarrow 1$) data. Nevertheless, the high spectral resolution of these data provides

TABLE 1
PHOTOMETRY DATA

Wavelength μm	Frequency GHz	Flux Density mJy	Instrument
		Combined/Unresolved	
1.25	239834	1.009 ± 0.09	2MASS/J-Band
1.65	181692	1.448 ± 0.12	2MASS/H-Band
2.17	138153	2.064 ± 0.16	2MASS/Ks-Band
3.4	88174.2	7.027 ± 0.14	*WISE*/W1
3.6	83275.7	5.618 ± 0.0021	*Spitzer*/IRAC
4.5	66620.5	7.803 ± 0.0021	*Spitzer*/IRAC
4.6	65172.3	8.872 ± 0.16	WISE/W2
5.8	51688.4	10.720 ± 0.0051	*Spitzer*/IRAC
8.0	37474.1	14.470 ± 0.0041	*Spitzer*/IRAC
12	24982.7	21.960 ± 0.42	WISE/W3
12	24982.7	<400	*IRAS*
22	13626.9	55.110 ± 1.9	WISE/W4
24	12491.4	70.204 ± 0.026	*Spitzer*/MIPS
25	11991.7	< 500	*IRAS*
60	4996.54	< 600	*IRAS*
100	2997.92	< 1000	*IRAS*
250	1199.17	289.4 ± 9.6	*Herschel*/SPIRE
350	856.55	168.2 ± 8.6	*Herschel*/SPIRE
500	599.585	56.8 ± 8.8	*Herschel*/SPIRE
1387.93	216	<2.492	CARMA
2152.82	139.256	1.230 ± 0.220	PdBI
		Foreground Lensing Galaxy	
0.555	540167	0.056 ± 0.006	*HST*-ACS/V-Band
0.814	368295	0.238 ± 0.013	*HST*-ACS/I-Band
1.6	187370	0.539 ± 0.041	*HST*-NICMOS(NIC2)/H-Band
3.6	83275.7	0.585 ± 0.003 [a]	*Spitzer*/IRAC
4.5	66620.5	1.794 ± 0.0027 [a]	*Spitzer*/IRAC
5.8	51688.4	3.163 ± 0.0059 [a]	*Spitzer*/IRAC
8.0	37474.1	4.589 ± 0.0057 [a]	*Spitzer*/IRAC
2152.82	139.256	0.799 ± 0.082	PdBI
61414	4.8815	0.866 ± 0.027	VLA
		Background Galaxy RXJ1131	
0.555	540167	0.009 ± 0.0041	*HST*-ACS/V-Band
0.814	368295	0.041 ± 0.0054	*HST*-ACS/I-Band
1.6	187370	0.133 ± 0.004	*HST*-NICMOS(NIC2)/H-Band
3.6	83275.7	5.034 ± 0.0021	*Spitzer*/IRAC
4.5	66620.5	6.009 ± 0.0017	*Spitzer*/IRAC
5.8	51688.4	7.557 ± 0.003	*Spitzer*/IRAC
8.0	37474.1	9.881 ± 0.0039	*Spitzer*/IRAC
2152.82	139.256	0.400 ± 0.082 [b]	PdBI
61414	4.8815	1.273 ± 0.042	VLA

REFERENCES. — The *HST* photometry is taken from C06.

NOTE. — The IRAC photometry for channel 1 (3.6 μm) is extracted directly from the image and from the Spitzer Heritage Archive for channels 2–4 (4.5, 5.8, and 8.0 μm). All upper limits are 3σ.
[a] Flux obtained using aperture photometry after subtracting the emission of RXJ1131 from the total emission.
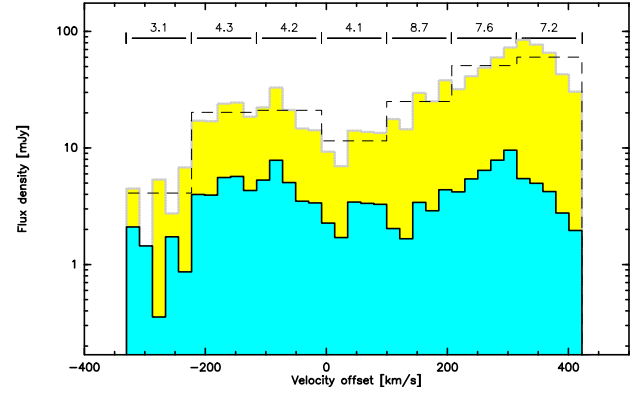[b] Flux extracted from the residual map after subtracting a point-source model.

FIG. 5.— The full resolution $CO(J = 2 \rightarrow 1)$ spectrum (yellow histogram) and the binned spectrum (dashed line) with the seven $\Delta v \sim 105\,km\,s^{-1}$ channels used for lens modeling. The blue histogram shows the "intrinsic" line profile of RXJ1131 after subtracting a contribution from its companion galaxy and correcting for lensing using the magnification factors μ_L as annotated by the horizontal bars shown above the respective model channels. Flux density on the y-axis is shown on a log scale.

dynamical information on spatial scales smaller than the beam (see Figure 2). Hence, we reconstruct the intrinsic gas dynamics by carrying out a parametric lens modeling over different channel slices of the interferometric data using our lensing code UVMCMCFIT (Bussmann et al. 2015a; see Bussmann et al. 2015b for details of the code). Models of each slice thus provide information on the corresponding kinematic component of the CO gas, enabling us to reconstruct the source plane velocity gradient. In order to have adequate SNRs for lens modeling, we bin the frequency channels by a factor of five to produce seven independent $\Delta v \sim 105\,km\,s^{-1}$ channels (dashed line in Figure 5) that cover the full linewidth of $\sim 750\,km\,s^{-1}$.

The lens mass distribution is modeled using a singular isothermal ellipsoid (SIE) profile, which is described by five free parameters: the positional offset in R.A. and Dec. relative to an arbitrary chosen fixed coordinate in the image, the Einstein radius, the axial ratio, and the position angle. We use the VLA radio continuum emission toward the foreground galaxy to initialize the positional offset. We impose a uniform prior $\pm 0.''05$ in both ΔR.A. and ΔDec., motivated by the astrometry uncertainties in the VLA image as well as the uncertainties provided by previous SIE lens model (C06). We initialize the Einstein radius based on the model parameters reported by C06 and impose a uniform prior using $\pm 3\sigma$ of their uncertainties. The sources are modeled using elliptical Gaussian profiles, which are parameterized by six free parameters: the positional offset in R.A. and Dec. relative to the lens, the intrinsic flux density, the effective radius, the axial ratio, and the position angle. The position of each source is allowed to vary between $\pm 1.''5$ (i.e., within the Einstein radius) and the effective radius is allowed to vary from $0.''01–2''$.

Our code uses an Markov Chain Monte Carlo (MCMC) approach to sample the posterior probability distribution function (PDF). In each model, we require a target acceptance rate of $\sim 0.25–0.5$ and check for chain convergence by inspecting trace plots and requiring the samples are beyond at least an autocorrelation time. We thus employ $\sim 50,000$ samples as the initial "burn-in" phase to stabilize the Markov chains (which we then discard) and use the final $\sim 5,000$ steps, sampled by 128 walkers, to identify the posterior. Here, we identify the best-fit model and the quoted uncertainties using the median and the 68% confidence intervals in the marginal PDFs.

We first obtain a preliminary lens model for each channel slice independently, where their lens parameters are allowed to vary and are initialized according to the aforementioned way. We obtain the final model by repeating the modeling over each slice but fixing their lens parameters to the overall median in the preliminary models, as listed in Table 2. This ensures that all models share the same lens profile. The magnification factors in Table 3 are

TABLE 2
LENS PARAMETERS CONSTRAINED BY
MODELS OF SEVEN VELOCITY CHANNELS

Parameters		Median values
Offset in RA	($''$)	0.004 ± 0.027
Offset in Dec	($''$)	0.003 ± 0.027
Axial Ratio		0.56 ± 0.16
Position Angle	(deg)	103 ± 22
Einstein Radius	($''$)	1.833 ± 0.002

NOTE. — Parameters describing the foreground lens are obtained based on the median in the preliminary models (see text for details). All angular offsets are with respect to $\alpha = 11^{\rm h}31^{\rm m}51\fs44$, $\delta = -12°31'58\farcs3$ (J2000).

TABLE 3
MAGNIFICATION FACTORS OF VARIOUS KINEMATIC
COMPONENTS IN CO($J = 2 \rightarrow 1$)

Velocity Range (km s^{-1})	Source 1 $\mu_{\rm L}$	Source 2 $\mu_{\rm L}$
-366 − -258	3.1 ± 0.9	
-237 − -151	4.3 ± 2.4	
-129 − -43	4.2 ± 0.6	
-21.5 − 65	4.1 ± 0.9	
86 − 172	8.7 ± 2.0	
194 − 280	7.6 ± 1.6	
301 − 388	7.2 ± 5.6	6.7 ± 2.5
weighted average	4.4	
median	5.5	

NOTE. — Velocity is taken from the center of each (native) channel without any binning. Each row corresponds to a channel slice used for lens modeling. Source 1 is RXJ1131 and source 2 is its companion. See text for details.

determined by taking the ratio between the image plane flux and the source plane flux of each model.

Our model parameters in Table 2, describing the mass distribution of the lensing galaxy, are consistent (within the uncertainties) with that of the SIE model presented by C06. We find a mass of $M(\theta < \theta_{\rm E}) = (7.47 \pm 0.02) \times 10^{11} \, M_\odot$ within the Einstein radius.

5.1.1. *Interpretation of the Source-plane Morphology*

The reconstructed source locations in Figure 6 demonstrate an intrinsic velocity gradient across the source plane, which is consistent with a kinematically-ordered disk-like galaxy. Additional support to the disk conjecture can be found in the double-horned line profile (Figure 1) and the observed (image plane) velocity field (Figure 2). Furthermore, C06 also find that the reconstructed source plane emission in optical-NIR is best-reproduced using a $n = 1$ Sersic profile. We thus interpret RXJ1131 as a disk galaxy.

A better fit is found for the lens model of the red-most channel if we add a second source component (see top left panel in Figure 6). This is consistent with previous results reported by Brewer & Lewis (2008, hereafter B08), who find an optically faint companion (component F in their paper) ~ 2.4 kpc in projection from the AGN host galaxy in V-band, and with C06, who find evidence for an interacting galaxy near RXJ1131. Spatially, the red velocity component of the CO emission also coincides with this component F. It is therefore likely that we detect CO($J = 2 \rightarrow 1$) emission in a companion galaxy.

The type of merger (major v.s. minor) in a pair of interacting galaxies is most commonly distinguished based on the ratio between their total galaxy mass. Here, we use the gas mass ratio between RXJ1131 and its companion galaxy instead, given that we do not have constraints on their individual galaxy mass. We decompose the total line flux into two components: one from RXJ1131 and the other from its companion. Since the companion is only detected in the red-most channel, we derive its intrinsic gas mass using the best-fit flux densities and magnification factors obtained from the models of this channel. Assuming a brightness temperature ratio of $r_{21} = 1$ between CO($J = 2 \rightarrow 1$) and CO($J = 1 \rightarrow 0$) lines and a CO luminosity-to-H$_2$ mass conversion factor of $\alpha_{\rm CO} = 0.8 \, M_\odot$ (K km pc^2)$^{-1}$, we find a molecular gas mass of $M_{\rm gas} = (1.92 \pm 0.09) \times 10^9 \, M_\odot$. For the molecu-

lar gas mass in RXJ1131, we derive its intrinsic line flux over the FWZI linewidth using the respective magnification factors listed in Table 3, which to first order takes into account effect of differential lensing. This yields $I_{\rm CO(J=2\rightarrow1)} = 2.93 \pm 0.70$ Jy km s^{-1}, where the uncertainty includes those on the magnification factors. Adopting the same brightness temperature ratio and $\alpha_{\rm CO}$ as used for the companion, this corresponds to a gas mass of $M_{\rm gas} = (1.38 \pm 0.33) \times 10^{10} \, M_\odot$, which implies a *gas* mass ratio of $\sim 7:1$ between RXJ1131 and its companion. We thus classify the system to be a *"wet-wet" minor merger*. We caution that this is based on their gas mass ratio rather than their total galaxy mass ratio, which is more commonly used in literature as the classification scheme to separate major mergers from minor mergers.

The spatial resolution of the data in hand is a few arcsec, which implies that despite the high SNR and spectral resolution, constraints on the intrinsic sizes of the lensed galaxies are modest, and thus the magnification factors may be under-predicted.

5.1.2. *Spatial Extent and Differential Lensing*

In the image plane shown in Figure 2, the redshifted component is cospatial with the Einstein ring seen in the optical image, with most of its apparent flux originating from the lensed arc in the southeast, whereas the blue component is predominately coming from solely the lensed arc. To further illustrate this, we show the channel maps of 21.5 km s^{-1} width and a spatial spectra map of $1\farcs5$ resolution in Figure 7 and Figure 8, respectively. The figures show that emission is present to the west, peaking toward the lensing arc (black crosses in Figure 7) in the red wing, and shifts to the east with decreasing velocity (blue wing). This is consistent with the source plane positions in our models and is suggestive of an extended CO emitting region.

Similar to previous studies of RXJ1131, where differential lensing across *HST V*-, *I*-, and *H*-band has been detected with a magnification factor decreasing from 10.9 to 7.8 (C06), the highly asymmetric CO($J = 2 \rightarrow 1$) line profile suggests that differential lensing is also non-negligible for CO, causing the redshifted emission to be apparently
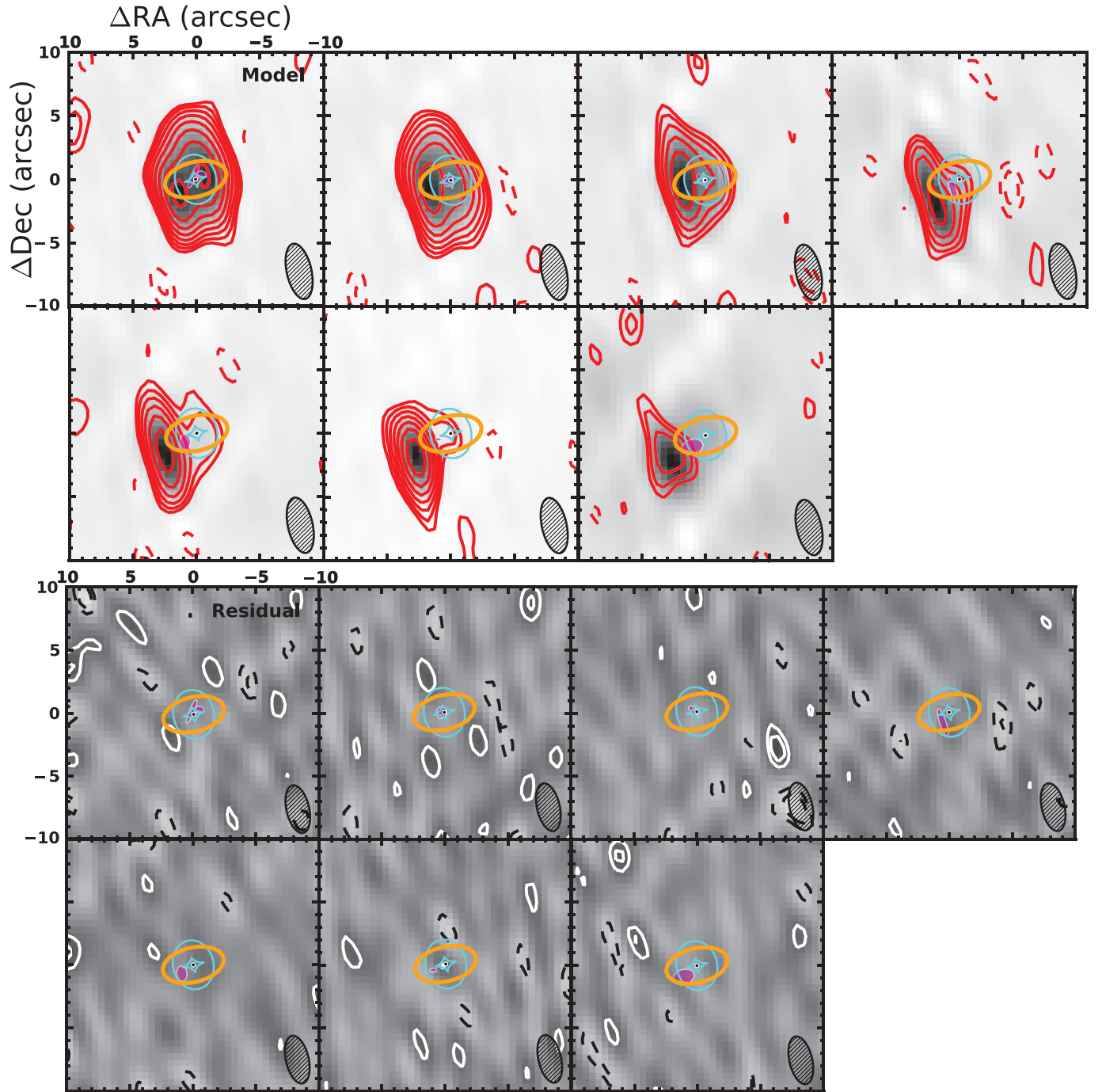
FIG. 6.— Each panel corresponds to a lens model of RXJ1131 performed over a channel slice $\sim$100 km s^{-1} of the CO($J = 2 \to 1$) data. Top: channel maps of the PdBI CO($J = 2 \to 1$) emission (red) overlaid on our best-fit lens models (grayscale). The location of the foreground lensing galaxy is indicated by a black dot and its critical curve is traced by the orange solid line. The locations and morphologies (half-light radii) of the reconstructed sources are represented by magenta ellipses. The caustic curves are represented as cyan lines. The beam of the PdBI observations is shown in the bottom right corner of each panel. Bottom: residual images of the best-fit models, obtained by taking the Fourier transform after subtracting the best-fit model from the data in the uv-domain. Contours start at $\pm 3\sigma$ and increment at steps of $3 \times 2^n \sigma$, where n is a positive integer.
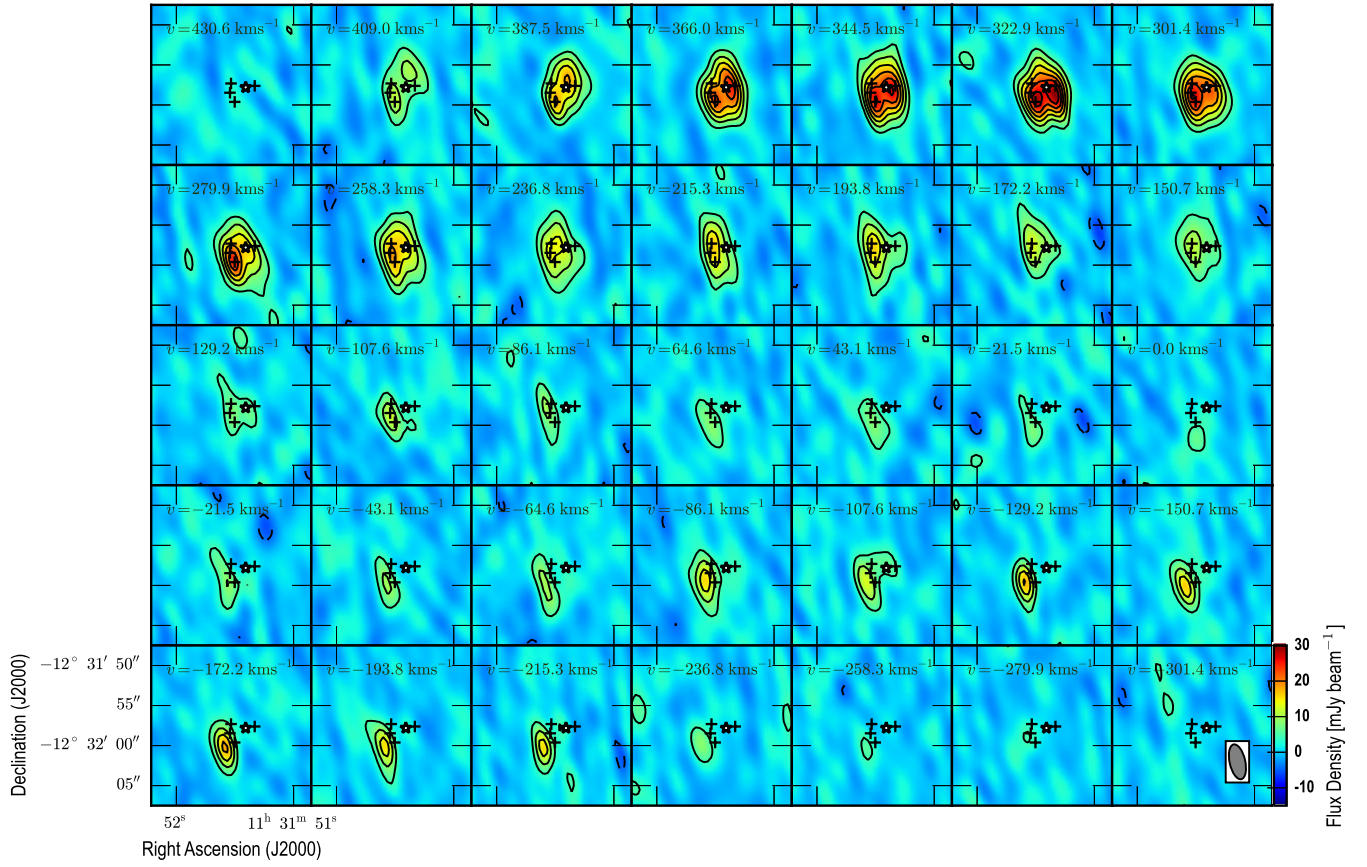
FIG. 7.— Channel maps of the PdBI CO($J = 2 \rightarrow 1$) data cube toward RXJ1131 at 21.5 km s^{-1} resolution. Black crosses indicate the positions of the lensed knots (AGN emission, which correspond to components ABCD in C06). The central white-filled star indicates the position of the foreground lensing galaxy (component G in C06). Central velocities are shown at the top of each map. Contours start and increment at steps of $\pm 3\sigma$. The beam is denoted in the bottom right panel.
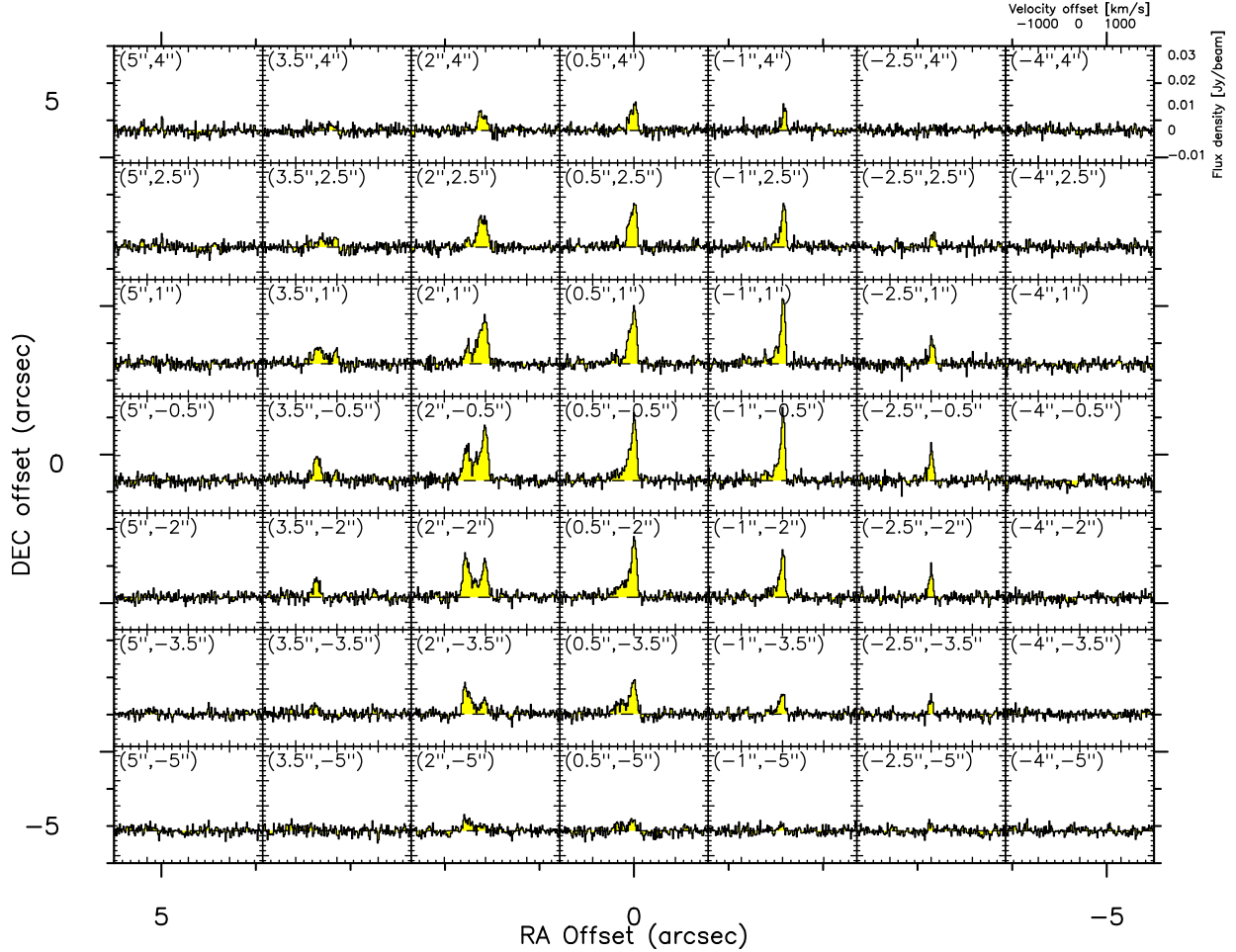
FIG. 8.— CO($J = 2 \rightarrow 1$) spectrum as a function of position, binned by 3 pixels in each direction ($1\rlap{.}''5$). The spectra map covers an extent of $\sim 10'' \times 10''$ centered on the pixel that corresponds to the lensing galaxy. Spatial offset in arcsec is denoted in top left corner of each panel. The velocity and flux density scales are denoted in the top right panel.

much brighter than the blueshifted component and the asymmetric line profile. This can be explained by the difference in magnification factor (μ_L) which varies from 8.7 to 3.1 across the CO($J = 2 \rightarrow 1$) line (Table 3) and also partly due to a contribution from the companion in the redshifted velocity channels. The variation in μ_L across channels is consistent with the source plane positions relative to the caustics in Figure 6, where the red wing emission mainly originates near the cusp of the caustic and the blue wing emission is located beyond the caustics. In fact, the intrinsic line flux of the redshifted and blueshifted emission in RXJ1131 (after subtracting a contribution from the companion) is $I_{\mathrm{CO}(J=2\rightarrow1)} = 1.26 \pm 0.23$ Jy km s^{-1} and 1.25 ± 0.23 Jy km s^{-1}, respectively, implying an intrinsically symmetric line profile (Figure 5). This is consistent with the source-plane velocity gradient in our lens model (Figure 6 and Figure 9).

5.2. CO(J = 2 → 1) Kinematics

Fitting a four-parameter double-Gaussian that describes two velocity peaks by a single FWHM to the "intrinsic" CO($J = 2 \rightarrow 1$) line profile of RXJ1131 (after correcting for lensing using the magnification factors for various channels and separating the emission from RXJ1131

and its companion), we find a roughly symmetric double-horned profile with a flux ratio of 1.2 ± 0.4 between the peaks, which are separated by $\Delta v_{\mathrm{sep}} = 387 \pm 45$ km s^{-1}, and a FWHM of 220 ± 72 km s^{-1}. The peak separation obtained from this "intrinsic" line profile is slightly lower than that obtained from the observed spectrum (i.e., without lensing corrections). This discrepancy is likely a result of differential lensing, which causes the line peak of the red wing to shift towards higher velocity channels, biasing the centroid of one of the components in a double-Gaussian to higher velocity than otherwise. If we instead fit with a single-Gaussian, we find a FWHM of 600 ± 160 km s^{-1} for RXJ1131 and 73 ± 43 km s^{-1} for the companion galaxy.

A clear velocity gradient and a high velocity dispersion ($\gtrsim 400$ km s^{-1}) near the central region is seen in Figure 2. While beam smearing is inevitably the dominant factor in the observed velocity dispersion at the spatial resolution of these data, the exceedingly high velocity dispersion may hint at potential perturbations from the AGN, or internal turbulence due to interactions with the companion, and/or instability due to the large gas content. Therefore, in this scenario, RXJ1131 is consistent with a disrupted disk galaxy hosting an optically bright quasar and is in the

process of merging.

5.3. CO(J = 2 → 1) Dynamical Modeling

Assuming the velocities of the respective channels used in the lens modeling correspond to solely the tangential component of the true velocity vector of a rotating disk (i.e., along the major axis), we extract a one dimensional PV diagram in Figure 9 by slicing across their source plane positions (PA: 121°).

We then attempt to characterize the molecular gas kinematics using an empirically-motivated disk model (e.g., Courteau 1997; Puech et al. 2008; Miller et al. 2011):

$$V = V_0 + \frac{2}{\pi} V_a \arctan(\frac{R}{R_t}), \qquad (1)$$

where V is the observed velocity, V_0 is the velocity at dynamical center, V_a is the asymptotic velocity, and R_t is the "turnover" radius at which the rotation curve becomes flat. We perform non-linear least square fitting using an orthogonal distance regression to find the best-fit parameters, taking into account the uncertainties in both velocity (channel width) and distance offset. We also place an upper limit on $R_t < 15$ kpc to keep this parameter physical (e.g., Puech et al. 2008; Miller et al. 2011). The parameter uncertainties are inferred based on a Monte Carlo simulation of 500 iterations, where the input parameters are perturbed according to random Gaussian distributions of sigmas corresponding to their uncertainties. Using this model, we find $V_a = 975 \pm 387$ km s^{-1}, $R_t = 10.7 \pm 5.7$ kpc, and $V_0 = 28 \pm 40$ km s^{-1}. However, since emission is not resolved along the flat regime of the rotation curve, the asymptotic velocity is poorly constrained and the "turnover" radius is at most an upper limit. In particular, V_a and R_t are highly correlated with a Pearson coefficient $R = 0.998$, and 0.027 between V_a and V_0.

The asymptotic velocity (V_a) – an extrapolation of the model out to radius beyond the disk scale-length and half-light radius – is not equivalent to maximum observed velocity (V_{max}), which is commonly used in literature to parameterize disk rotation. The arctangent model is most commonly used in studies of the Tully-Fisher relation, where an extrapolation to V$_{2.2}$ (velocity at 2.2 disk scale-length or ~ 1.375 half-light radius, or $\sim 0.7 R_{opt}$[5]) is typically adopted as the rotation velocity (V_{max} in their terminology) since this corresponds to the radius at which the velocity of a pure exponential disk peaks (Courteau & Rix 1997). We here adopt the maximum *observed* velocity $V_{rot} = 345 \pm 55$ km s^{-1} at 6 ± 3 kpc from the dynamical center as a proxy to the rotation velocity. This radius corresponds to $\sim 0.6 R_e$, where R_e is the half-light radius ~ 10.3 kpc inferred from the *HST I*-band lens model (C06; converted to our cosmology). We note that the source plane half-light radius varies substantially with wavelength. In particular, the half-light radius is found to be ~ 4 kpc and ~ 7 kpc in *V*-band (B08) and *H*-band (C06), respectively. The CO gas is thus of similar spatial extent as in *H* and *I*-bands.

---

[5] Radius enclosing 83% of the light distribution.

In the rest-frame, emission in the observed-frame *H*-band corresponds to NIR emission ($\sim 1 \mu$m), tracing radiation from the accretion disk surrounding the central AGN and also from old and evolved stellar populations; *I*-band corresponds to roughly the optical *V*-band, tracing stellar radiation from existing, less massive (i.e., longer-lasting) stars; *V*-band corresponds to roughly *U*-band, tracing radiation from massive young stars in the host galaxy. Hence, the *V*-band compactness may be explained in part due to the fact that its emission is more susceptible to dust extinction than in other bands and/or a central starburst caused by higher concentrations of star-forming gas towards the central regions – owing to gravitational perturbations induced from interactions with the companion (e.g., Di Matteo et al. 2005). This is consistent with the picture that old stars form first and constitute the bulge component of a spiral galaxy and that nuclear starbursts (in the inner few kpc) can be triggered in a later time as the progenitor disk galaxy interacts with other galaxies, and thereby forming a larger bulge.

5.4. SED Modeling

We fit dust SED models to the 24 μm−2.2 mm photometry in Figure 10, where we also include the IRAS 60 μm and 100 μm upper limits to constrain the dust peak. The fit is performed with the code MBB_EMCEE (e.g., Riechers et al. 2013; Dowell et al. 2014), which samples the posterior distributions using an MCMC approach and uses instrumental response curves to perform color correction on-the-fly. The SED model consists of a modified-blackbody function with a power-law attached to the Wien side to account for an excess in the MIR owing to emission of warm and small dust grains. The model is thus described by five free parameters: the rest-frame characteristic dust temperature (T_d), the emissivity index (β), the power-law index (α), the flux normalization at 500 μm (f_{norm}), and the observed-frame wavelength at which the emission becomes optically thick (λ_0). We impose a uniform prior with an upper limit of 100 K on T_d (see e.g., Sajina et al. 2012), a Gaussian prior centered around $\mu = 1.9$ with $\sigma = 0.3$ on β, and a uniform prior with an upper limit of 1000 μm on λ_0. We check for chain convergence by requiring that the autocorrelation length of each parameter is less than the number of steps taken for the burn-in phase (which are then discarded). Here we report the statistical means and the 1σ confidence interval in the marginal PDFs as the best-fit parameters, as listed in Table 4.

In the first model, we include the 24 μm data to constrain the power-law index. Based on the best-fit of this model, we find an apparent far-IR luminosity (rest-frame $42.5 − 122.5 \mu$m) of $3.81^{+2.04}_{-1.92} \times 10^{12} L_\odot$ and a dust mass of $22^{+5}_{-18} \times 10^8 M_\odot$, uncorrected for lensing. For the mass absorption coefficient, we adopt $\kappa = 2.64$ m^{2}kg^{-1} at rest-frame 125.0 μm (Dunne et al. 2003). The dust mass uncertainty does not include that of the absorption coefficient.

A fit including the MIR 24 μm photometry is likely an upper limit on the far-IR luminosity due solely to star formation in the AGN host galaxy. If we instead fit for a model excluding this constraint, two major consequences
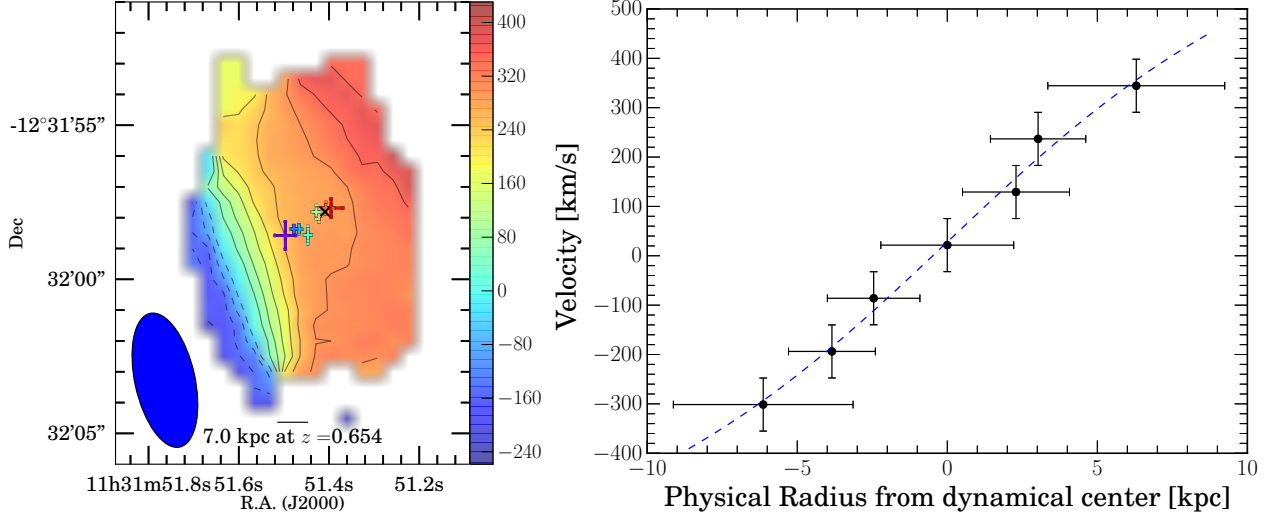
FIG. 9.— Left: Source-plane positions from best-fit CO($J = 2 \rightarrow 1$) lens models are indicated with their associated uncertainties atop the observed first moment map. The contours are at steps of 50 km s^{-1}. Right: PV slice along the major axis in the source plane at PA = 121°. Dashed line shows the best-fit rotation curve using an arctangent model. The vertical error bars show the channel width for each model and the horizontal error bars are the 1σ uncertainties on the source plane positions.

TABLE 4
SED FITTING RESULTS

Parameters		With 24μm	Without 24μm
T_d	(K)	$52.0^{+4.0}_{-4.1}$	$58.2^{+14.5}_{-14.4}$
β		$1.8^{+0.5}_{-0.6}$	$2.1^{+0.3}_{-0.3}$
α		$1.6^{+0.5}_{-0.5}$	$8.9^{+6.9}_{-6.3}$
λ_0 [a]	(μm)	548^{+285}_{-307}	367^{+125}_{-145}
λ_{peak} [b]	(μm)	162^{+16}_{-30}	146^{+39}_{-44}
$f_{norm, 500\mu m}$ [c]	(mJy)	59^{+14}_{-13}	60^{+5}_{-5}
L_{FIR} [d]	($10^{12} L_\odot$)	$3.81^{+2.04}_{-1.92}$	$4.72^{+2.54}_{-2.26}$
M_d [e]	($10^8 M_\odot$)	22^{+5}_{-18}	11^{+5}_{-6}

NOTE. — Errors reported here are $\pm 1\sigma$. L_{FIR} and M_d are not corrected for lensing.

[a] Observed-frame wavelength where $\tau_\nu = 1$
[b] Observed-frame wavelength of the SED peak
[c] Observed-frame flux density at 500 μm
[d] Rest-frame 42.5–122.5 μm luminosity
[e] Derived assuming absorption mass coefficient of $\kappa = 2.64$ m^2 kg^{-1} at $\lambda = 125.0$ μm (Dunne et al. 2003)

are immediately apparent. First, the power-law index is poorly-constrained (see Table 4). Second, the steep power-law implies only a small contribution from the power-law regime to the total IR luminosity as compared to the graybody component. Thus, the far-IR luminosity in this model should, in principle, correspond to a lower limit on the cold dust emission. Using the best-fit parameters for this model, we find a total IR luminosity L_{IR} (rest-frame $8 - 1000$ μm) of $9.71^{+6.14}_{-6.05} \times 10^{12} L_\odot$, a far-IR luminosity L_{FIR} of $4.72^{+2.54}_{-2.26} \times 10^{12} L_\odot$ and a dust mass M_{dust} of $11^{+5}_{-6} \times 10^8 M_\odot$, all of which are uncorrected for lensing. Taken at face value, this implies a FIR-to-IR luminosity ratio of $\sim 58 \pm 35\%$.

The dust temperature from both models is similar to that of ULIRGs at $0.6 < z < 1.0$ (54 ± 5 K; Combes et al. 2013, hereafter C13). We note the far-IR luminosity is comparable in both models, which is not surprising given the lack

of constraints in the MIR. For the subsequent analysis, we adopt the physical quantities from the first model (i.e., with constraints at 24 μm). The choice of SED model does not affect the derived star formation rate (SFR) given the similar far-IR luminosity. Yet, the dust mass is higher by a factor of ~ 2 in the former but consistent within the uncertainties. We correct for lensing using the median magnification factor ($\mu_L = 5.5$) from the CO lens models. This yields a L_{FIR} of $(6.9 \pm 3.6) \times 10^{11} L_\odot$ and a total IR luminosity of $\sim 1.5 \times 10^{12} L_\odot$, implying RXJ1131 is a ULIRG. Assuming a Salpeter initial mass function (Salpeter 1955), we find a SFR$_{FIR}$ of $120 \pm 63 M_\odot$ yr^{-1} using a standard conversion (Kennicutt 1998).
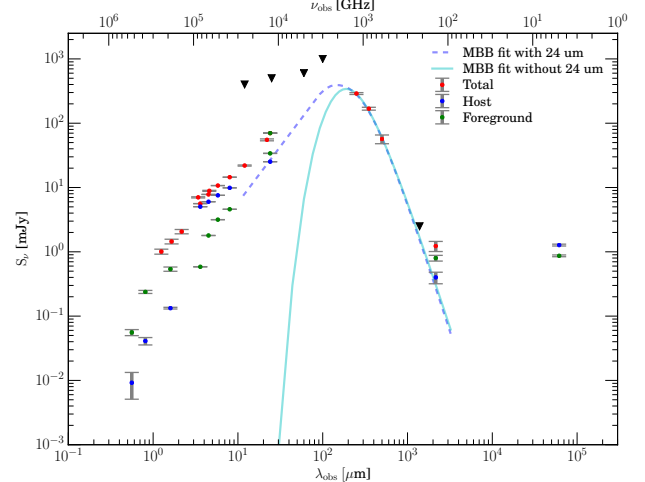

FIG. 10.— SEDs of RXJ1131 and its lensing galaxy. The photometry is listed in Table 1. Best-fit SED models of the thermal dust emission towards RXJ1131 with(out) MIR constraint at 24 μm are plotted as dashed (solid) lines.

5.5. ISM Properties

In this section, we derive the gas properties of the merging system based on CO($J = 2 \rightarrow 1$) and compare

them with those reported by C13 — the largest sample of ULIRGs at similar redshift ($0.6 < z < 1.0$) with CO measurements[6]. Their results are based on unresolved CO($J = 2 \rightarrow 1$) and CO($J = 4 \rightarrow 3$) line observations with the IRAM 30-m single-dish telescope.

5.5.1. *Linewidth and Sizes*

A FWHM linewidth of $\Delta v \sim 600 \pm 160 \, \mathrm{km \, s^{-1}}$ found for RXJ1131 by fitting a single Gaussian is considerably larger that those in the C13 sample ($370 \, \mathrm{km \, s^{-1}}$) as well as in local ULIRGs ($300 \pm 85 \, \mathrm{km \, s^{-1}}$, with the largest being $480 \, \mathrm{km \, s^{-1}}$; Solomon et al. 1997, hereafter S97). Yet, given the dynamic nature of these galaxies, a CO linewidth of $\sim 600 \, \mathrm{km \, s^{-1}}$ may not be surprising. Indeed, a linewidth of $\Delta v = 750 \, \mathrm{km \, s^{-1}}$ has been observed in a local LIRG (Arp 118; Solomon & Vanden Bout 2005, hereafter SV05). Linewidth of this range ($\gtrsim 500 \, \mathrm{km \, s^{-1}}$) is also commonly observed in high-z starburst galaxies (e.g., Greve et al. 2005, hereafter G05) and high-z quasar host galaxies (e.g., Coppin et al. 2008), which are believed to originate from mergers.

The CO gas in RXJ1131 is $\sim 6 \pm 3 \, \mathrm{kpc}$ in radius (in the source plane), which is more extended than the average in a sample of disk-like U/LIRGs studied by Ueda et al. (2014), but consistent with their range of $1.1 - 9.3 \, \mathrm{kpc}$. Our CO size is also consistent with that of high-z ($z > 1$) galaxies ($R \sim 4-20 \, \mathrm{kpc}$; G05; Daddi et al. 2010; Riechers et al. 2011; Ivison et al. 2011) and local U/LIRGs in the Gao & Solomon (1999) sample ($R \lesssim 10 \, \mathrm{kpc}$).

5.5.2. *Dynamical Mass*

Assuming the gas is virialized, the dynamical mass can be approximate as $M_{\mathrm{dyn}} = \sigma^2 R / G$, where σ is the velocity dispersion, or the rotational velocity in the case of a rotating disk model (i.e., $\sigma = V_{\mathrm{rot}} \sin i$). Using a rotational velocity $V_{\mathrm{rot}} \sin i = 345 \, \mathrm{km \, s^{-1}}$ (see §5.3), we find a dynamical mass of $M_{\mathrm{dyn}} \sin^2 i (< 6 \, \mathrm{kpc}) = 17 \times 10^{10} \, M_\odot$ enclosed within the CO-emitting region in RXJ1131. If we instead consider the CO($J = 2 \rightarrow 1$) line peak separation ($\Delta v_{\mathrm{sep}}/2 \sim 200 \, \mathrm{km \, s^{-1}}$) as the rotation velocity, we find $M_{\mathrm{dyn}} \sin^2 i (< 6 \, \mathrm{kpc}) = 5.8 \times 10^{10} \, M_\odot$. We derive an inclination angle of $56.4°$ from the morphological axial ratio of $a/b \sim 1\farcs8 / 3\farcs25$, which we estimate from the source-plane image reconstructed by C06 (Figure 3 in their paper). This corresponds to an inclination-corrected dynamical mass of $8.3 \times 10^{10} \, M_\odot < M_{\mathrm{dyn}} < 25 \times 10^{10} \, M_\odot$. Our estimate should be considered at best an upper limit since the gas in RXJ1131 is unlikely virialized. In the following sections, we use the lower limit $(8.3 \pm 1.9) \times 10^{10} \, M_\odot$ as the dynamical mass as it is derived in a manner similar to what is commonly used in literature (e.g., S97; Downes & Solomon 1998, hereafter DS98; G05).

Using the velocity dispersion obtained by fitting a single Gaussian to the line profile of the companion ($\sigma =$

$30 \, \mathrm{km \, s^{-1}}$) and its intrinsic source size of $\sim 700 \, \mathrm{pc}$ obtained from the *HST V*-band lens model (B08), we find a dynamical mass of $M_{\mathrm{dyn}} \sin^2 i = 1.5 \times 10^8 \, M_\odot$. This corresponds to $M_{\mathrm{dyn}} = 5.8 \times 10^8 \, M_\odot$ if we assume an inclination angle of $30°$. We adopt the *V*-band size as the radius R in the above estimate owing to the fact that it is the least uncertain constraint on the source size for the companion. However, since this dynamical mass is substantially lower than the gas mass, which is a more reliable estimate based on the data in hand, we do not use this dynamical mass to derive other physical parameters. The underestimated dynamical mass may reflect the dusty nature of the companion, which causes its *V*-band source size to appear much smaller than its true extent without any dust obscuration. If we use the half-right radius of $R_{\mathrm{CO}} = 4.2 \pm 2.8 \, \mathrm{kpc}$ obtained from our best-fit lens model as the unobscured source size (see §5.1.1), we find a dynamical mass of $M_{\mathrm{dyn}} = (3.5 \pm 2.3) \times 10^9 \, M_\odot$ (assuming $i = 30°$), which is physically more sensible than that derived using the *V*-band source size. The uncertainty here only includes that of the CO source size. Given the large systematic uncertainties associated with the model-based source size and the lack of constraint on the inclination angle, we do not use this dynamical mass in the remaining of this paper.

5.5.3. *Gas Mass and Gas Ratios*

Using the lensing-corrected dust mass, we find a galactic-scale gas-to-dust ratio of 40 ± 34, which is lower than the statistical average of $f_{\mathrm{gas-dust}} = 206$ in the C13 sample but well within their broad range of values over the entire sample. Our ratio is also consistent with high-z SMGs (Bothwell et al. 2013) and local ULIRGs (Wilson et al. 2008), but lower than of the Milky Way by $\sim 4\sigma$ (ignoring systematic uncertainties; Li & Draine 2001; Zubko et al. 2004; Draine et al. 2007). We note that the dust mass derived for RXJ1131 is poorly constrained. If we adopt a dust mass from the other SED fit (i.e., without constraints at $24 \, \mu\mathrm{m}$), the dust mass would reduce by a factor of ~ 2.

There are a number of systematic uncertainties associated with this quantity. For instance, the mass opacity coefficient κ, the α_{CO} conversion factor, and the brightness temperature ratio r_{21}. If we instead use the "Galactic" α_{CO} value, which may be more appropriate for some ULIRGs (e.g., Papadopoulos et al. 2012) and minor mergers (Narayanan et al. 2012), the gas mass (and thus gas-to-dust ratio) would be ~ 6 times higher. We note that this gas mass is physically feasible based on dynamical mass constraint. On the other hand, we would also obtain a higher gas mass if we assumed sub-thermal excitation between CO($J = 2 \rightarrow 1$) and CO($J = 1 \rightarrow 0$) emission, but we expect this to be a minor effect as CO emission in ULIRGs are thermalized up to $J = 3$ or 4. We also note that the gas-to-dust ratio derived for RXJ1131 maybe biased low as the gas is likely to be more extended than the dust. Consequently, the overall magnification factor for the CO gas may be lower than the optically thick dust, which dominates the far-IR luminosity, and thus leading to an overestimated dust mass via our adoption of the CO magnification factor.

5.5.4. *SFE and Depletion Timescales*

To first order, the star formation efficiency (SFE = L_{FIR}/M_{gas}) indicates the star formation rate per unit solar mass of molecular gas available in a galaxy. Using a wavelength range of $40-500\,\mu m$ defined in C13 as the far-IR luminosity, we find an SFE of $58 \pm 10\,L_{\odot}\,M_{\odot}^{-1}$, which is on the low end among other U/LIRGs at $z < 0.6$ (S97; Combes et al. 2011) but consistent with those of low-z spiral galaxies ($z < 0.1$; SV05) and high-z disk-like galaxies (Daddi et al. 2008). Assuming an α_{CO} of $0.8\,M_{\odot}$ (K km pc^2)$^{-1}$ is appropriate for RXJ1131, this would imply that it is converting gas into stars at an efficiency similar to those of "normal" star-forming disk-like galaxies rather than starburst galaxies (Tacconi et al. 2008; Riechers et al. 2011, C13). This is in agreement with its disk-like kinematic signatures.

Results from theoretical simulations have suggested that the disk component of a gas-rich progenitor galaxy can survive merging if it has a low star formation efficiency, which in turn reduces the gravitational torque available to remove the angular momentum of the gas, thereby allowing a higher gas fraction to be retained and redistributed over a large extent in the merged galaxy (Hopkins et al. 2009). With this, it is plausible that RXJ1131 will evolve into a disk galaxy with a small bulge component upon merging given its low SFE.

Assuming the star formation continues at the current rate without gas replenishment, this corresponds to a gas depletion time of $\tau = 102 \pm 25$ Myr. Since the star formation rate is expected to vary in an interacting system and AGN accretion also consumes some fraction of the gas, the depletion timescale should only be considered as an upper limit.

6. DISCUSSION

6.1. *Fate of RXS J1131−1231*

The classical picture for mergers is one where they are responsible for the formation of the local red and passive spheroidal galaxies. With more realistic treatments of star formation and feedback in recent simulations, it has been suggested that it is possible to suppress bulge formation in gas-rich mergers, thereby forming large disks that resemble local spiral galaxies (Springel & Hernquist 2005; Robertson et al. 2006; Hopkins et al. 2009). The extended molecular gas distribution in RXJ1131 together with its low SFE implies that the removal of angular momentum of the gas via gravitational torque is inefficient. Other mechanisms e.g. bar-like structures that are more efficient at removing angular momentum will be required in order to transform the gas disk of RXJ1131 into a stellar spheroid and evolve into an E/S0 galaxy. Without these, it is more conceivable that RXJ1131 will retain its disk component and evolve into a disk galaxy upon its final coalescence with the companion.

6.2. *Velocity Offset and a Recoiling Black Hole*

Using the CO line center redshift as the systemic redshift, we find a velocity offset of $\sim780\,\mathrm{km\,s^{-1}}$ from the optical MgII 2798Å line and the [OIII] 4959, 5007Å lines ($z_{\mathrm{QSO}} = 0.658$; S03). This implies that the AGN is dynamically offset from the centroid of its host galaxy. From the CO channel maps in Figure 2 and Figure 7, it is also apparent that the line center of the gas is not co-spatial with the optical quasar as the point-like images along the lensing arc are spatially offset to the NW of the CO line center. While spatial offsets between optical lines and CO line have been reported in other galaxies, the velocity offsets are typically $\lesssim 500\,\mathrm{km\,s^{-1}}$. **In the classical SDSS analysis for line offsets (Richards et al. 2002)?. [OIII] 4959, 5007Å and MgII 2798Å analysis (Boroson 2005; Bae & Woo 2014)?. with the corresponding trends and possible explanations?. More extreme offsets between CO and optical lines have been seen (Hainline et al. 2004) or between [CII]and MgII 2798Å (e.g., Venemans et al. 2016).** For instance, the velocity offset in an SDSS sample of ongoing mergers at $z < 0.21$ is at most ~410 km/s (Comerford & Greene 2014).

A large velocity offset can also result from a recoiling black hole (BH) where its broad line region is moving at high velocity relative to the bulk of its host galaxy (Madau & Quataert 2004; Bonning et al. 2007; Loeb 2007). Such a scenario is expected to occur when a pair of uneven mass BH coalesce, during which their orbital energy is being released as gravitational wave and a non-zero net angular momentum is being carried away. Depending on their initial conditions, numerical relativity simulations have shown that the recoil velocity can reach up to $\sim4000\,\mathrm{km\,s^{-1}}$ for spinning BHs (e.g., Campanelli et al. 2007). The fact that the BH in RXJ1131 has a high spin parameter (Reis et al. 2014) renders this scenario a viable option for the origin of the velocity offset. However, since this model requires a merged BH, this interpretation would imply RXJ1131 have already encountered with the companion galaxy, which is consistent with the highly spinning BH observed in RX1131. Given the presence of a nearby companion observed in our data, the system may be in its subsequent stages of (minor) merging resulting from previous passage of a major merger.

As demonstrated here using MgII 2798Å and [OIII] 4959, 5007Å lines, large velocity offsets between CO and optical lines may be present. We thus caution against the use of optical lines as true systematic redshift indicators as the resulting redshift can deviate from the true value.

6.3. *The $M_{\mathrm{BH}}-M_{\mathrm{dyn}}$ Relation*

Assuming RXJ1131 follows the local $M_{\mathrm{BH}}-M_{\mathrm{bulge}}$ relation reported by Häring & Rix (2004), the virial-based black hole mass $M_{\mathrm{BH}} \sim 6\times10^7\,M_{\odot}$ (Peng et al. 2006) corresponds to a stellar bulge mass of $M_{\mathrm{bulge}} = 4.2\times10^{10}\,M_{\odot}$. This implies that the bulge component is responsible for making up roughly half the dynamical mass. If we subtract the black hole mass, gas mass, and dust mass[7] from the dy-

---

[7] Here, we adopt the lowest dust mass among the two SED models to derive an upper limit on the stellar mass.

namical mass and ignore a contribution from the dark matter, this would yield an upper limit on the stellar mass of $6.8 \times 10^{10} \, M_\odot$. Thus, the bulge mass derived above based on the local relation is not physically infeasible. The stellar mass upper limit would also imply a lower limit on the $M_{\rm BH}/M_{\rm bulge}$ ratio of $\sim 0.09\%$, which falls below the local relation but is consistent within the range found in other intermediate-z radio-loud AGNs (McLure et al. 2006). A dark matter fraction of over $f_{\rm DM} \sim 0.6$ would be needed for RXJ1131 to lie above the local relation and fall outside the range of $M_{\rm BH}/M_{\rm bulge}$ found in (McLure et al. 2006).

6.4. *Dynamical lens modeling of high-z quasars*

Riechers08a is the only other similar system at emission in host galaxy lensed into an Einstein ring configuration and with dynamical lens modeling of CO. Which also velocity gradient. Constraints on the.

6.5. *Others*

Comparing the spatial extents of the CO with the stellar components traced by *HST*
The dusty nature of this system??
compare to Riechers08a
= compare to J04135 in R13

7. SUMMARY AND CONCLUSIONS

We observe CO($J = 2 \to 1$) and CO($J = 3 \to 2$) line emisison toward the quadruply-lensed quasar RXJ1131 at $z_{\rm CO} \sim 0.65$ using the PdBI and CARMA, benchmarking the first resolved interferometric CO imaging at intermediate redshift. The brightness temperature ratio between CO($J = 2 \to 1$) and CO($J = 3 \to 2$) of r_{32} = BLAH, which taking into account the large phase errors associated with CO($J = 3 \to 2$) , is consistent with thermalized excitation between these lines in other ULIRGs. The (gas) mass ratio, the intrinsic CO line profile, and the source-plane velocity field are all evident of a minor merger, in good agreement with previous studies of RXJ1131 in the optical (C06; B08).

The intrinsically symmetric double-horned line profile, the smooth and symmetric velocity field/gradient seen in both the source plane from our lens model as well as in the image plane are characteristics resembling a rotating disk, consistent with the findings from previous optical lens model. The high dispersion $\gtrsim 400 \, \mathrm{km \, s^{-1}}$ near the dynamical center suggest that RXJ1131 is turbulent, albeit lack of spatial resolution. Our lens modeling analysis also confirms the presence of the optically faint companion suggested by previous studies, with CO emission. Assuming the same CO excitation as RXJ1131 for the companion, we find a gas mass of BLAH, which implies a gas mass ratio of ($\sim 7{:}1$) between RXJ1131 and the companion. We thus classify the system is a wet minor merger. We conclude that RXJ1131 is a ULIRG hosting a massive gas reservoir in a disturbed/turbulent disk, undergoing merging with a nearby companion (aka a wet minor merger).

While many characteristics of RXJ1131 resembles local ULIRGs and high-z SBs (such as linewidth, CO sizes, SFR, gas mass), its SFE is similar to that nearby spiral galaxies and high-z disk-like galaxies rather than ULIRGs or high-z starbursts galaxies at $z \gtrsim 0.6$. Our result is consistent with the emerging consensus on the correlation between molecular gas content and redshift, suggesting it as the explanation for the elevated SFR at high redshift/ the observed trend in the cosmic SFH. Given our large error bar on the gas mass fraction, we cannot constrain its evolution but our result is consistent with a decreasing trend of gas fraction since $z \approx 1.0$ (Combes et al. 2013); but is consistent with in both ULIRGs samples in redshift bins of $0.2 < z < 0.4$ and $0.6 < z < 1.0$ within the uncertainties.

The compact UV emission, which can be a starburst resulting from gas accumulation owing to a non-axisymmetric perturbation from the companion. Dusty nature of companion? The IR luminosity also agrees with the results from previous low-z studies: AGNs are typically found in late stage mergers (Yuan et al. 2010; Iwasawa et al. 2011; Carpineti et al. 2012) and only major mergers near their final coalescence can provide $L_{\rm IR} > 10^{12} \, L_\odot$, (e.g., Carpineti et al. 2015; Larson et al. 2016). In contrast to the galaxies with ULIRG-like IR luminosity at high redshifts, which can be in early stages of merging.

We find that the optical lines are offset from the systemic redshift by $\sim 780 \, \mathrm{km \, s^{-1}}$, (caution use of optical lines as systemic redshift) may imply a recoiling black hole in RXJ1131, which would imply the black holes (and their host galaxies) have merged or are at their final coalescence. The highly spinning black hole in RXJ1131 is also consistent with this hypothesis. Given the presence of a companions, it is plausible that RXJ1131 is in its late stage of merging and possibly encountered with its companion previously, consistent with compact SB traced by V-band image triggered by gas inflow/accumulation toward nuclear regions arising from perturbations in the disk from/interactions with the companion. Theoretical simulations suggest disk in progenitor galaxy may be retained post-merging in gas-rich mergers. BLAH. Thus, the merging system studied here will likely evolve into a merged disk galaxy.

The use of dynamical mass as a proxy to the $M_{\rm BH} - \sigma_*$ have been proposed in a few high-z studies but requires resolved observations to provide constraints on the spatial extent tracing the potential of the host galaxy. Lensing likely the the way to allow observations of quasar emission and host galaxy emission. Dynamical lens modeling provides a promising avenue to study the velocity structure and dynamics of the cold gas in greater detail. To date, only a few other studies using similar techniques e.g., other luminous, gas-rich interacting galaxies and mergers. This study of RXJ1131 serves as a benchmark/demonstrate the use of gravitational lensing and dynamical lens modeling for further high-resolution molecular gas studies at intermediate redshifts. Similar resolved CO studies are needed to investigate the evolution in the $M_{\rm BH} - M_{\rm dyn}$ relation to understand the co-evolution of SMBHs and their host galaxies through cosmic time.

Alexander, D. M., Brandt, W. N., Smail, I., et al. 2008, AJ, 135, 1968
Astropy Collaboration, Robitaille, T. P., Tollerud, E. J., et al. 2013, A&A, 558, A33
Bae, H.-J., & Woo, J.-H. 2014, ApJ, 795, 30
Bonning, E. W., Shields, G. A., & Salviander, S. 2007, ApJ, 666, L13
Boroson, T. 2005, AJ, 130, 381
Borys, C., Smail, I., Chapman, S. C., et al. 2005, ApJ, 635, 853
Bothwell, M. S., Smail, I., Chapman, S. C., et al. 2013, MNRAS, 429, 3047
Brewer, B. J., & Lewis, G. F. 2008, MNRAS, 390, 39
Bussmann, R. S., Leung, T. K. D., & Conley, A. 2015a
Bussmann, R. S., Riechers, D., Fialkov, A., et al. 2015b, ApJ, 812, 43
Campanelli, M., Lousto, C. O., Zlochower, Y., & Merritt, D. 2007, Physical Review Letters, 98, 231102
Carilli, C. L., & Walter, F. 2013, ARA&A, 51, 105
Carpineti, A., Kaviraj, S., Darg, D., et al. 2012, MNRAS, 420, 2139
Carpineti, A., Kaviraj, S., Hyde, A. K., et al. 2015, A&A, 577, A119
Claeskens, J.-F., Sluse, D., Riaud, P., & Surdej, J. 2006, A&A, 451, 865
Combes, F., García-Burillo, S., Braine, J., et al. 2011, A&A, 528, A124
—. 2013, A&A, 550, A41
Comerford, J. M., & Greene, J. E. 2014, ApJ, 789, 112
Coppin, K. E. K., Swinbank, A. M., Neri, R., et al. 2008, MNRAS, 389, 45
Courteau, S. 1997, AJ, 114, 2402
Courteau, S., & Rix, H.-W. 1997, in Bulletin of the American Astronomical Society, Vol. 29, American Astronomical Society Meeting Abstracts, 1332
Daddi, E., Dannerbauer, H., Elbaz, D., et al. 2008, ApJ, 673, L21
Daddi, E., Bournaud, F., Walter, F., et al. 2010, ApJ, 713, 686
Dai, X., Kochanek, C. S., Chartas, G., et al. 2010, ApJ, 709, 278
Di Matteo, T., Springel, V., & Hernquist, L. 2005, Nature, 433, 604
Dowell, C. D., Conley, A., Glenn, J., et al. 2014, ApJ, 780, 75
Downes, D., & Solomon, P. M. 1998, ApJ, 507, 615

Draine, B. T., Dale, D. A., Bendo, G., et al. 2007, ApJ, 663, 866
Dunne, L., Eales, S. A., & Edmunds, M. G. 2003, MNRAS, 341, 589
Erb, D. K., Steidel, C. C., Shapley, A. E., et al. 2006, ApJ, 646, 107
Fazio, G. G., Hora, J. L., Allen, L. E., et al. 2004, ApJS, 154, 10
Gao, Y., & Solomon, P. M. 1999, ApJ, 512, L99
Greve, T. R., Bertoldi, F., Smail, I., et al. 2005, MNRAS, 359, 1165
Hainline, L. J., Scoville, N. Z., Yun, M. S., et al. 2004, ApJ, 609, 61
Häring, N., & Rix, H.-W. 2004, ApJ, 604, L89
Hinshaw, G., Larson, D., Komatsu, E., et al. 2013, ApJS, 208, 19
Hopkins, A. M., & Beacom, J. F. 2006, ApJ, 651, 142
Hopkins, P. F., Cox, T. J., Younger, J. D., & Hernquist, L. 2009, ApJ, 691, 1168
Ivison, R. J., Papadopoulos, P. P., Smail, I., et al. 2011, MNRAS, 412, 1913
Iwasawa, K., Sanders, D. B., Teng, S. H., et al. 2011, A&A, 529, A106
Kennicutt, Jr., R. C. 1998, ARA&A, 36, 189
Larson, K. L., Sanders, D. B., Barnes, J. E., et al. 2016, ArXiv e-prints, arXiv:1605.05417
Li, A., & Draine, B. T. 2001, ApJ, 554, 778
Loeb, A. 2007, Physical Review Letters, 99, 041103
Madau, P., & Dickinson, M. 2014, Cosmic Star-Formation History
Madau, P., & Quataert, E. 2004, ApJ, 606, L17
Magorrian, J., Tremaine, S., Richstone, D., et al. 1998, AJ, 115, 2285
McLure, R. J., Jarvis, M. J., Targett, T. A., Dunlop, J. S., & Best, P. N. 2006, MNRAS, 368, 1395
Miller, S. H., Bundy, K., Sullivan, M., Ellis, R. S., & Treu, T. 2011, ApJ, 741, 115
Narayanan, D., Krumholz, M. R., Ostriker, E. C., & Hernquist, L. 2012, MNRAS, 421, 3127
Neugebauer, G., Habing, H. J., van Duinen, R., et al. 1984, ApJ, 278, L1
Ott, S. 2010, in Astronomical Society of the Pacific Conference Series, Vol. 434, Astronomical Data Analysis Software and Systems XIX, ed. Y. Mizumoto, K.-I. Morita, & M. Ohishi, 139
Papadopoulos, P. P., van der Werf, P., Xilouris, E., Isaak, K. G., & Gao, Y. 2012, ApJ, 751, 10

Peng, C. Y., Impey, C. D., Rix, H.-W., et al. 2006, ApJ, 649, 616

Pooley, D., Blackburne, J. A., Rappaport, S., & Schechter, P. L. 2007, ApJ, 661, 19

Puech, M., Flores, H., Hammer, F., et al. 2008, A&A, 484, 173

Reis, R. C., Reynolds, M. T., Miller, J. M., & Walton, D. J. 2014, Nature, 507, 207

Richards, G. T., Vanden Berk, D. E., Reichard, T. A., et al. 2002, AJ, 124, 1

Riechers, D. A., Hodge, J., Walter, F., Carilli, C. L., & Bertoldi, F. 2011, ApJ, 739, L31

Riechers, D. A., Walter, F., Brewer, B. J., et al. 2008, ApJ, 686, 851

Riechers, D. A., Bradford, C. M., Clements, D. L., et al. 2013, Nature, 496, 329

Rieke, G. H., Young, E. T., Engelbracht, C. W., et al. 2004, ApJS, 154, 25

Robertson, B., Bullock, J. S., Cox, T. J., et al. 2006, ApJ, 645, 986

Sajina, A., Yan, L., Fadda, D., Dasyra, K., & Huynh, M. 2012, ApJ, 757, 13

Salpeter, E. E. 1955, ApJ, 121, 161

Skrutskie, M. F., Cutri, R. M., Stiening, R., et al. 2006, AJ, 131, 1163

Sluse, D., Surdej, J., Claeskens, J.-F., et al. 2003, A&A, 406, L43

Solomon, P. M., Downes, D., Radford, S. J. E., & Barrett, J. W. 1997, ApJ, 478, 144

Solomon, P. M., & Vanden Bout, P. A. 2005, ARA&A, 43, 677

Springel, V., & Hernquist, L. 2005, ApJ, 622, L9

Stern, D., Eisenhardt, P., Gorjian, V., et al. 2005, ApJ, 631, 163

Tacconi, L. J., Genzel, R., Smail, I., et al. 2008, ApJ, 680, 246

Ueda, J., Iono, D., Yun, M. S., et al. 2014, ApJS, 214, 1

Venemans, B. P., Walter, F., Zschaechner, L., et al. 2016, ApJ, 816, 37

Walter, F., Carilli, C., Bertoldi, F., et al. 2004, ApJ, 615, L17

Walter, F., Decarli, R., Sargent, M., et al. 2014, ApJ, 782, 79

Wilson, C. D., Petitpas, G. R., Iono, D., et al. 2008, ApJS, 178, 189

Wright, E. L., Eisenhardt, P. R. M., Mainzer, A. K., et al. 2010, AJ, 140, 1868

Yuan, T.-T., Kewley, L. J., & Sanders, D. B. 2010, ApJ, 709, 884

Zubko, V., Dwek, E., & Arendt, R. G. 2004, ApJS, 152, 211